Exploring the Atomic-Scale Interactions at the Interface of Reducible Oxide and Ruthenium Nanocatalyst in Ammonia Decomposition

Mansu Kim[a,*], Jian Liu[a,b], Jonghwan Park[c], Sohui Kim[c], Kunmo Koo[d], Vinayak P. Dravid[d], Dongmok Whang[c], and Joseph T. Hupp[a,*]

[a]*Department of Chemistry, Northwestern University, 2145 Sheridan Road, Evanston, Illinois 60208, United States*

[b]*School of Chemistry and Materials Science, Rochester Institute of Technology, 84 Lomb Memorial Drive, Rochester, New York 14623, United States*

[c]*School of Advanced Material Science and Engineering, Sungkyunkwan University, 2066 Seobu-ro, Suwon, Gyeonggi-do, 16419, Republic of Korea*

[d]*Department of Materials Science and Engineering, Northwestern University, Evanston, IL 60208, United States*

[*]Corresponding author

E-mail: j-hupp@northwestern.edu (J. T. Hupp), mansu.kim@northwestern.edu (M. Kim)

Keywords: support interaction, reducible oxide, ruthenium catalyst, metal-organic framework, ammonia decomposition

Abstract

Reconstructing interfaces at the atomic level through interactions between precious metal catalysts and highly stable oxides opens new possibilities for enhancing inherent catalytic properties. Here, we investigate the interactions between metal oxide particles and Ru nanoparticles formed through the pyrolysis of metal-organic frameworks (MOFs) composed of oxide clusters with varying reducibility, accompanied by Ru precursor ions in an oxygen-suppressed, high-temperature environment. This study utilizes the ammonia decomposition reaction as a probe to examine these interactions. Despite having an ideal size of 2.3 nm for ammonia decomposition, Ru nanoparticles interacting strongly with reducible CeO_2 nanoparticles exhibit relatively low conversion rates. Post-catalysis, X-ray absorption spectroscopy (XAS) analysis reveals changes at the interface between CeO_2 and Ru particles, shedding light on the correlation between the electron occupancy of Ru nanoparticles and their catalytic activity for ammonia decomposition.

Introduction

Reconstructing nanostructured catalysts using minimal quantities of precious nanoparticles supported on stable oxide substrates has become a focal strategy in nanocatalysis. Such strategies are motivated by the potential to induce strong metal-support interactions, which are pivotal for enhancing catalytic efficiency and stability.[1] Particularly, supports like chemically robust ZrO_2, when interfaced with sub-nanometric particles,[2] can facilitate significant alterations in the electronic structure through electron perturbations at the interface.[3] These modifications in the electronic structure are critical as they influence both the chemical stability of the catalyst and the adsorption energy of reactants.[4] Traditional impregnation methods, while facilitating metal-support interactions through the gradual reduction of catalysts at very low concentrations,[5] are often inadequate for achieving high-density binding of catalysts on oxide surfaces. In contrast, infiltrating precursor metal ions into metal-organic frameworks (MOFs) and employing simple pyrolysis procedures have been shown to effectively restructure at the atomic level, resulting in stable oxide-based catalysts.[6] The inherent non-catalytic nature of metal oxide clusters forming the regular periodic nodes in MOFs has often led to their exclusion from major influential roles;[7] however, upon undergoing pyrolysis, uniformly distributed oxide nanoparticles have demonstrated the capacity to form interfaces with spatially confined heteroatoms on the support, thereby impacting the catalyst's electronic structure.[6]

Ammonia (NH_3) serves as an effective energy carrier,[8] and enhancing the chemical conversion efficiency of catalysts necessary for the ammonia decomposition process is essential for viable applications.[9] Ruthenium (Ru) is a representative catalyst located at the peak of the Volcano curve, effectively balancing energy through the continuous dehydrogenation of adsorbed NH_3 molecules, leading to the conversion into N_2 and H_2.[10] The rate-determining step of ammonia decomposition on the catalyst surface, the recombinative desorption of nitrogen,[10] is influenced by factors such as particle size, crystal structure, and alloy formation, which all impact the electronic structure of catalyst.[11] Typically, the optimal size for Ru particles is known to be about 2.3 nm,[12] though this can vary depending on the type of support and its interactions.[13] For instance, Ru/CNT catalysts,[14] where Ru particles under 2 nm are synthesized on CNT supports, demonstrate high activity due to effective electron transfer from the CNT interface.[15] In contrast, despite having the same size Ru particles, different tendencies are observed on various oxide supports,[13] highlighting that the influence of support interactions is as significant as the absolute size of Ru particles.

Herein, we investigate how the activity of ammonia decomposition varies according to the interactions between Ru nanoparticles and oxide supports with different reducibility. The Ru nanoparticle-based catalysts are prepared by simple pyrolysis of precursor Ru ions infiltrated into MOFs under a high-temperature environment suppressed of oxygen. The synthesized MOFs, encompassing three types of metal oxide nodes, exhibit distinctly different tendencies in particle distribution and interactions post-pyrolysis, based on properties such as MOF structure and chemical adsorption. Notably, despite Ru-CeO_2/C having a relatively higher Ru mass content and nearly ideal particle size of 2.3 nm, it shows a lower conversion rate for ammonia decomposition compared to catalysts supported on other types of oxides. This is attributed to the strong interactions at the interface where the highly reductive CeO_2 impacts the catalytic activity by influencing electron occupancy on Ru nanoparticles. The changes at the interface between Ru particles and the oxide surface, induced by strong interactions, are elucidated through extended X-ray Absorption Fine Structure (EXAFS) analysis of the electronic structure of catalysts after the ammonia decomposition reaction. Further understanding of the catalyst-support interactions driven by the electronic occupancy of the Ru catalyst according to the reducibility of metal oxides will provide clear insights into designing effective catalysts for ammonia decomposition.

Results and discussion

Ru-based catalysts for ammonia decomposition, containing nanoparticles of three different transition metal oxides, were synthesized through high-temperature annealing of MOFs with Ru precursor ions in an environment where oxygen was completely suppressed. The Hf- and Zr-based MOFs utilized a cubic structure of UiO-66, and their crystalline structure as white powders was confirmed via Powder X-ray Diffraction (PXRD) (Figure S1).[16] Scanning Electron Microscopy (SEM) images (Figure 1a, b) showed relatively uniform particle sizes exceeding 250 nm and the typical cubic morphology of UiO-66.[17] The Ce-based MOF appeared as a slightly yellowish white powder and was identified as a triclinic structure Ce-1,4 benzenedicarboxylic acid (BDC) MOF in XRD analysis.[18] SEM images (Figure 1c) displayed rod-shaped formations with a thickness of approximately 500 nm. Interestingly, Brunauer-Emmett-Teller (BET) measurements (Figure S2a) revealed distinct differences in the surface areas of these materials. Hf- and Zr-based MOFs showed typical type I isotherm curves with surface areas of 628 and 1085 m²/g, respectively.[17] Hf-UiO-66 typically exhibited a lower surface area compared to Zr due to the relatively higher atomic weight of Hf. In contrast, the Ce-MOF, nearly identical to values reported in other literature, displayed a very low surface area of 10 m²/g with a minimal N_2 isotherm curve.[18] This was attributed to the chemical adsorption of the BDC linker, acetic acid and dimethylformamide (DMF) on the Ce^{3+} nodes in the Ce-BDC MOF,[19-20] which likely reduced the available areas for N_2 adsorption, resulting in a significantly lower surface area.[18]

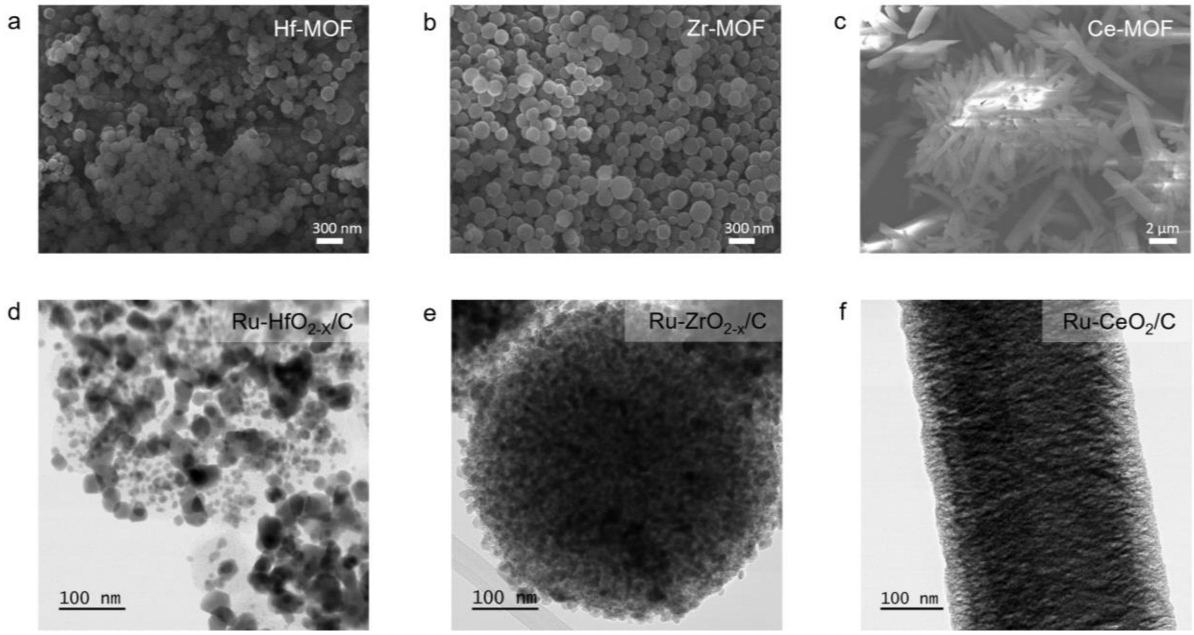

Fig. 1. SEM images displaying the morphologies of MOFs before pyrolysis: (a) Hf-MOF, (b) Zr-MOF, (c) Ce-MOF. TEM images illustrating changes in morphology after pyrolysis and the formation of metal oxide nanoparticles: (d) $Ru\text{-}HfO_{2\text{-}x}/C$, (e) $Ru\text{-}ZrO_{2\text{-}x}/C$, (f) $Ru\text{-}CeO_2/C$.

Despite its low specific surface area, the Ce-MOF rapidly absorbed Ru ion precursors, similar to other MOFs, and surprisingly, the powder remained very buoyant in vials, suggesting that the effective surface area could be much higher than measured, akin to other samples. After impregnation and filtering, the powder displayed a uniformly dark brown color and was subsequently subjected to pyrolysis under high-purity argon gas at 950 °C. After pyrolysis, three samples of the Ru-impregnated MOFs were designated as Ru-metal (Me)O_2-x/C. The N_2 isotherm analysis (Figure S2b) showed surface areas of 275 m²/g and 326 m²/g for $Ru\text{-}HfO_{2\text{-}x}/C$ and $Ru\text{-}ZrO_2$-x/C, respectively, while $Ru\text{-}CeO_2/C$ demonstrated a higher surface area of approximately 113 m²/g compared to the Ce-MOF. This increase can be attributed to the desorption of chemicals strongly bound to Ce^{3+} and the partial oxidation state transition from

Ce^{3+} to Ce^{4+} during pyrolysis, which likely weakened the chemical bonding to the newly formed Ce^{4+}. However, a small portion of Ce^{3+} that remains after pyrolysis forms strong chemical bonds with atmospheric CO_2,[21] contributing to a lower surface area compared to other materials. Transmission electron microscopy (TEM) images (Figure 1d) of the Ru-HfO_{2-x}/C sample revealed that the spherical-shaped MOF structures had collapsed into agglomerated black particles of HfO_{2-x}, formed on the carbon support from the degraded organic ligands, with particles showing irregular sizes and distribution. In contrast, TEM images of Ru-ZrO_{2-x}/C exhibited relatively uniform, large particles, preserving the original spherical shape of the Zr-MOF distributed on carbon. Meanwhile, the Ru-CeO_2/C maintained the rod-like shape of the Ce-MOF, with particles being very small and uniformly distributed throughout the porous carbon.

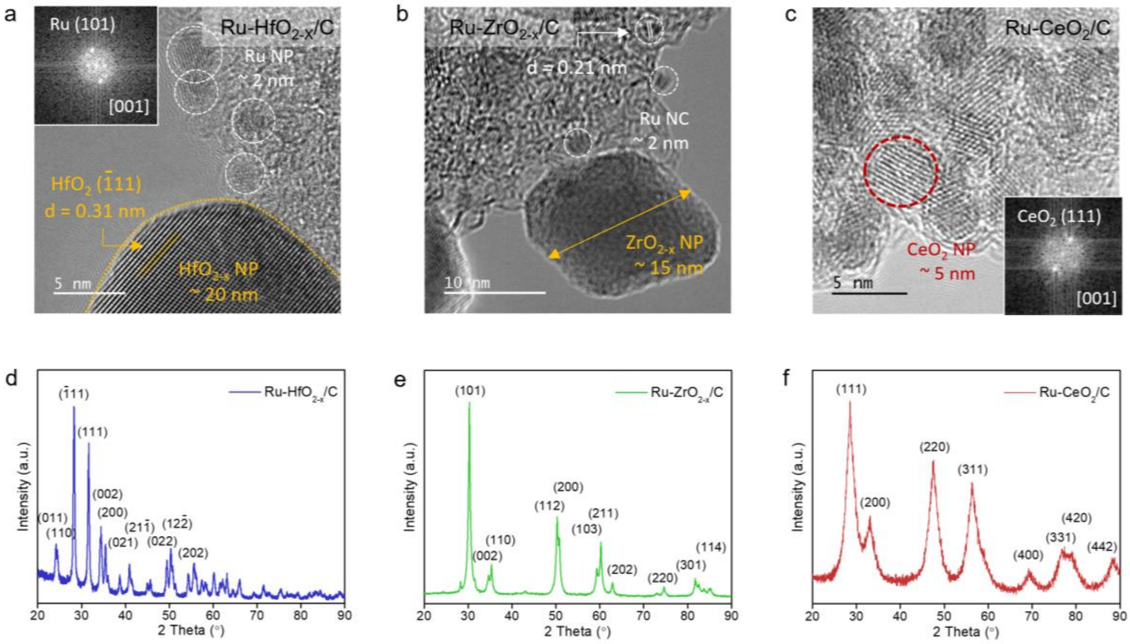

Fig. 2. HR-TEM images showcasing: (a) Ru-HfO_{2-x}/C with insets displaying FFT patterns of localized regions, illustrating Ru (101) lattice, (b) Ru-ZrO_{2-x}/C, highlighting the structure of Ru NCs, and (c) Ru-CeO_2/C, with a close-up on CeO_2 NPs and the corresponding FFT pattern inset. XRD patterns: (d) for Ru-HfO_{2-x}/C, (e) Ru-ZrO_{2-x}/C, and (f) Ru-CeO_2/C.

High-resolution (HR)-TEM images (Figures 2a-c) provided a more detailed examination of the crystal structures and particle sizes of three types of catalysts. Particles smaller than 2 nm in size (average size 1.83 nm), not observed in low-magnification TEM images of Ru-HfO_{2-x}/C, were identified as hexagonal close-packed (hcp) structured metallic Ru nanoparticles, as confirmed by the corresponding fast Fourier transform (FFT) patterns (Figures 2a and S3a).[22] Larger particles over 20 nm exhibited a monoclinic (m) structure of HfO_2, with lattice spacing of 0.31 nm, matching the prominent peak (-111) in the XRD pattern of Ru-HfO_{2-x}/C (Figure 2d).[23] These smaller, less crystalline Ru particles relative to HfO_2-x NPs were challenging to identify in XRD due to a lack of corresponding peaks. Similarly, Ru particles under 2 nm in size (average = 1.65 nm, Figure S3b) were very uniformly dispersed on the carbon surface, with their lattice spacing of 0.21 nm matching the metallic hcp Ru (101).[24] ZrO_2-x particles of 15 nm were identified as tetragonal ZrO_2 (101) from their lattice spacing (d = 0.3 nm) and FFT patterns (Figure S3b), matching the tetragonal structure ZrO_2 peak (101) in the XRD pattern (Figure 2e). The structural differences between HfO_2-x and this could be attributed to the phase stability of t-ZrO_2, which can remain stable at room temperature for crystal sizes under 17 nm;[25] in contrast, undoped ZrO_2 typically shows a tetragonal phase above 1000°C and transitions to m-ZrO_2 at room temperature.[26] Post-thermal treatment, the HfO_2-x particles exceeded 20 nm, suggesting that the size influences these structural differences. In the case of Ru-CeO_2/C, CeO_2 particles were under 5 nm, making them difficult to distinguish from Ru particles in HR-TEM image (Figure 2c). However, Ru particles were identified using STEM-EDS (scanning transmission electron microscopy energy-dispersive X-ray spectroscopy) mapping in dark-field TEM images, with an average size of 2.35 nm, typically less than 3 nm (Figure S4). CeO_2 in Ru-CeO_2/C exhibited a cubic structure (Figure 2f), and unlike the other two XRD peaks which arose from small particle size and low crystallinity, the broad peak types were consistent with the XRD peak for CeO_2 (111) confirmed from the FFT pattern obtained from the TEM image (Figure 2c, inset).[27]

The size and dispersion trends of Ru nanoparticles and other metal oxide particles during the pyrolysis of MOFs containing three different transition metals can be categorized into two distinct pathways. In a high-temperature environment with well-suppressed oxygen, the pyrolysis of MOFs structured with face-centered cubic (fcu) featuring Zr_6 or Hf_6 oxide cluster nodes containing Ru precursor ions leads predominantly to carbothermal reduction.[28] This process involves the organic ligands of the MOF being converted into conductive carbon supports while simultaneously stripping oxygen atoms from the surrounding oxide clusters to reduce the precursor Ru ions and form CO.[28] Furthermore, during the carbothermal reduction process, the loss of oxygen from Zr_6 (or Hf_6) oxide clusters leads to the formation of oxygen vacancies and the partial reduction of metal cations.[28] So, in the oxygen-suppressed, high-temperature conditions, the rapid consumption of carbon from organic ligands in MOFs during carbothermal reduction leads to a loss of carbon surface that would otherwise support the oxide particles after pyrolysis. This results in easier mobility of the oxide clusters, thus producing more disordered and larger oxide particles as observed in the Hf-MOF after pyrolysis, which tend to protrude from the surface of the carbon support (Figures 1d,e). X-ray photoelectron spectroscopy (XPS) analysis confirms this mechanism, showing partial reduction from oxidation state +4 to +3 in the core-level peaks of Hf 4f and Zr 3d spectra (Figures 3a,b).[29-30] Additionally, the O1s spectra (Figure 3d) indicate a higher percentage of oxygen vacancies at 29.7% (Ru-HfO_{2-x}/C) and 29.9% (Ru-ZrO_{2-x}/C) compared to the Ru-CeO_2/C sample,[31] aligning with the discussed trends.

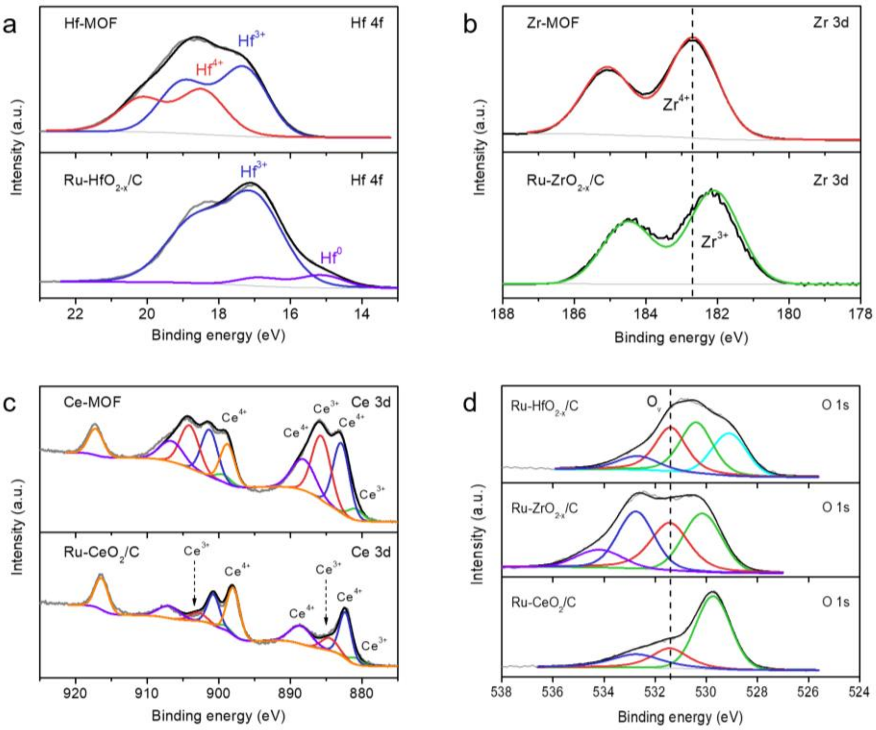

Fig. 3. XPS spectra of (a) Hf 4f of Hf-MOF and Ru-HfO_{2-x}/C, (b) Zr 3d of Zr-MOF and Ru-ZrO_{2-x}/C, (c) Ce 3d of Ce-MOF and Ru-CeO_2/C, (d) O 1s of Ru-HfO_{2-x}/C (top), Ru-ZrO_{2-x}/C (middle), Ru-CeO_2/C (bottom).

In the case of Ce-MOF with a triclinic structure containing Ru precursors, the pyrolysis process demonstrated a distinct trend. Post-pyrolysis, the XPS Ce 3d core-level peaks (Figure 3c) showed a significant decrease in the ratio of Ce^{4+} to Ce^{3+}.[32] In the oxygen-suppressed high-temperature environment, it is predicted that Ce oxide clusters composed of Ce^{3+}, which form strong bonds with carboxyl groups such as BDC linker, acetic acid and DMF, would leave one oxygen atom and release the other as CO gas,[33] forming CeO_2 particles. Therefore, the XPS O 1s spectra (Figure 3d) revealed a relatively low oxygen vacancy percentage (21.5%). This distinct behavior of Ce-MOF was also evident in its low specific surface area measured by the BET analysis and observed in the thermogravimetric analysis (TGA) curves (Figure S5). The TGA curves showed a sharp mass decrease near 80°C for Hf-MOF and Zr-MOF, primarily associated with the removal of water and other solvents.[34] The gentle decline in mass up to 500°C suggests a gradual thermal degradation of the MOF ligands, followed by a significant loss at higher temperatures due to complete ligand degradation and carbonization. In contrast, the very low BET results for Ce-MOF suggest extremely strong adsorption of CO_2 and H_2O around the Ce^{3+} nodes and within the pores, resulting in only a minimal mass loss of less than 10% up to 200°C, likely due to the release of strongly bound water molecules and a small amount of adsorbed CO_2. Post-200°C, the mass reduction followed a similar trajectory to Zr-MOF, indicating partial degradation of the BDC linkers, with a similar rapid decrease in mass occurring at comparable temperatures post-500°C, likely due to complete degradation and carbonization of the BDC linkers. Interestingly, post-600°C, unlike the other two samples, Ce-MOF exhibited a sharp mass decrease exceeding 20%, likely due to the high-temperature environment causing the Ce^{3+} clusters to release adsorbed CO_2 in the form of CO gas and grow into larger crystals, suggesting that the strong adsorption by Ce^{3+} hindered the sintering process, leading to relatively smaller CeO_2 particle sizes.

Following the pyrolysis of MOFs containing Ru precursor ions and three different types of metal oxide cluster nodes, the differences in catalyst performance for ammonia decomposition reactions were evaluated to understand the interaction between the Ru nanoparticles and the type of oxide supports. Temperature screening tests for ammonia decomposition were conducted by flowing 10 ccm of 10% NH_3 gas at a heating rate of 1°C/min up to 700°C, showing an onset reaction temperature near 350°C and complete conversion around 500°C (Figure 4a). At a fixed temperature of 400°C and during a time-on-stream of 12 hours, the catalysts displayed similar stable conversion rates as initially observed (Figure 4b). Inductively coupled plasma optical emission spectrometry (ICP-OES) analysis (Table S1) revealed that the Ru content in the Ru-ZrO_{2-x}/C catalyst was 1.4 wt%, which exhibited the highest conversion rate in Figure 4b. However, the Ru-HfO_{2-x}/C catalyst, with a Ru content of 1.1 wt%, displayed a higher turnover frequency (TOF) of 0.027 s^{-1} compared to 0.018 s^{-1} for Ru-ZrO_{2-x}/C, determined by the slope in Figure 4c. This higher efficiency is attributed to the larger Ru particle size of 1.83 nm in Ru-HfO_{2-x}/C, which is more suitable for ammonia decomposition than the 1.65 nm particles in Ru-ZrO_{2-x}/C. Notably, the Ru-CeO_2/C catalyst, containing the highest Ru concentration of 1.7 wt%, showed the lowest conversion rate and TOF of 0.010 s^{-1}, despite having an ideal Ru particle size of 2.35 nm for ammonia decomposition. This suggests that, even with an optimal particle size,[12] other factors related to support interaction of catalyst and the environment within the MOF structure can significantly influence catalytic activity.

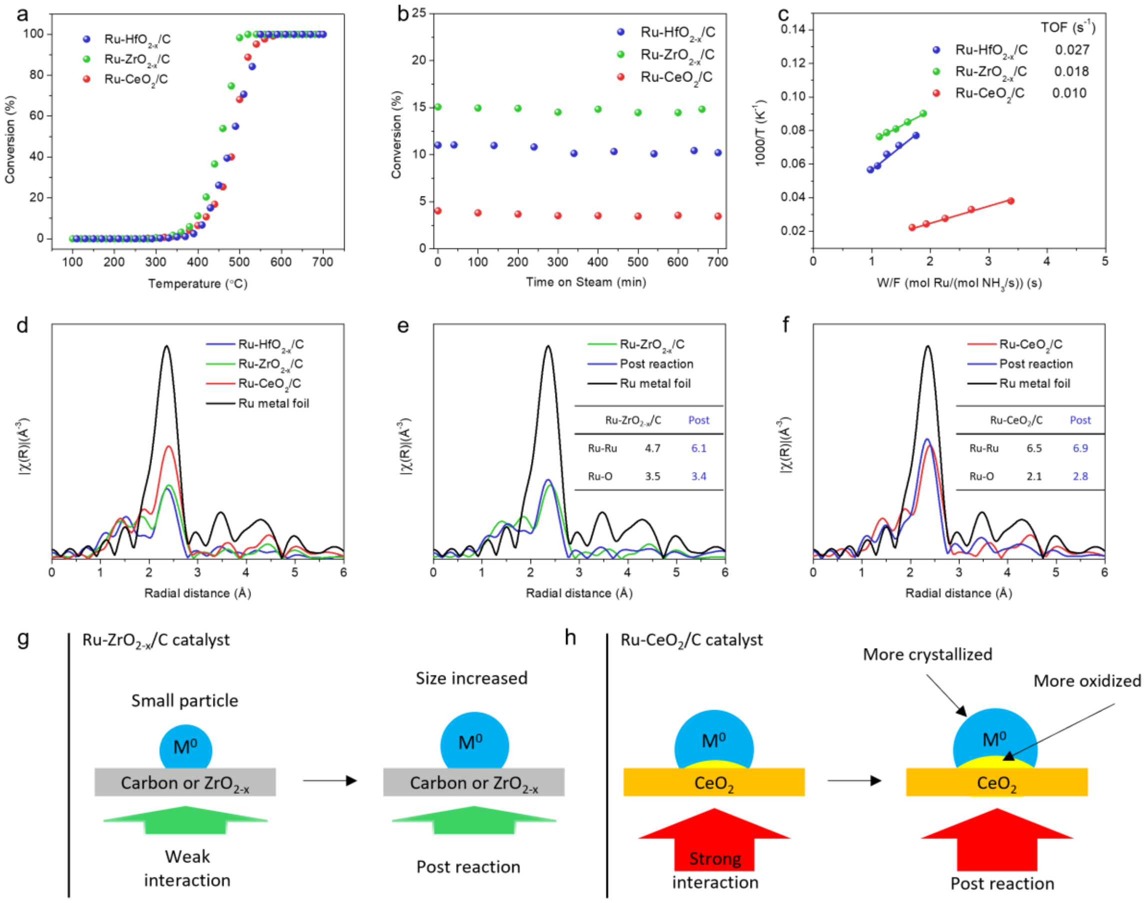

Fig. 4. Catalytic decomposition of ammonia of Ru catalysts on different oxide supports: (a) Temperature-dependent conversion rates; (b) Stability tests at 400 °C (c) Ammonia conversion versus ammonia space velocity (W/F, where W is the amount of Ru in moles and F is the flow rate of ammonia in mol/s) at 400 °C. The FT k^2-weighted $\chi(k)$-functions from Ru-EXAFS spectra are shown for (d) Ru-HfO_{2-x}/C, Ru-ZrO_{2-x}/C, Ru-CeO_2/C; (e) Ru-ZrO_{2-x}/C and post-reaction states; (f) Ru-CeO_2/C and post-reaction states. Schematics illustrating the interaction mechanisms between the metal and support for (g) Ru-ZrO_{2-x} and post reaction, and (h) Ru-CeO_2 and post reaction.

To elucidate the complex relationships between catalyst structure and ammonia decomposition reaction, we examined the crystal structures of the catalysts using Fourier transform k^2-

weighted χ(k)-functions from Ru extended X-ray absorption fine structure (EXAFS) spectra. The first shell minor shoulder peaks around 1.99 Å correspond to Ru-O interactions, and the main peaks near 2.67 Å were identified as Ru-Ru bonds (Figure 4d).[33] The fitting results of Ru-EXAFS spectra (Figure S6) highlighted that the Ru-CeO_2/C sample exhibited a distinctly prominent Ru-Ru peak with a coordination number of 6.5, significantly higher compared to 4.7 in the Ru-ZrO_{2-x}/C sample. This suggests that the larger Ru particle size, resulting from a higher Ru content, may account for this difference (Table 2). Post-ammonia decomposition, the coordination number for Ru-Ru in the Ru-ZrO_{2-x}/C sample increased significantly from 4.7 to 6.1, indicating that the high-temperature environment and the production of hydrogen gas during ammonia decomposition likely facilitated the sintering of smaller Ru particles, leading them to agglomerate independently on the porous carbon surface away from the larger ZrO_{2-x} particles (Figure 4g). Conversely, the Ru-CeO_2/C sample showed a slight increase in the Ru-Ru coordination number from 6.5 to 6.9, and interestingly, the Ru-O bonding also significantly increased from 2.1 to 2.8 (Figures 4f and S7, Table 3). This suggests a close and strong interaction between Ru and CeO_2 particles during ammonia decomposition, which might explain why the Ru-CeO_2/C catalyst, despite having the largest and most abundant metallic Ru particles, exhibited the lowest efficiency in the ammonia decomposition process. The strong interaction with the reducible oxide; CeO_2 and partial electron loss likely impacted its ammonia decomposition rate. The proximity of Ru particles to CeO_2 during the decomposition process and the increasing occupied interface could account for the increased Ru-O bonding. Although the Ru-CeO_2/C catalyst exhibited lower activity for ammonia decomposition, exploring the metal-support interactions facilitated by MOFs and understanding the variations in interactions based on the type of metal oxide used hold promising potential for various energy applications. Specifically, this approach could contribute significantly to the development of new concepts for oxide-based catalysts with enhanced stability.

Conclusions

We conducted pyrolysis of metal-organic frameworks (MOFs) composed of oxide clusters with varying reducibility and containing Ru precursor ions, under an oxygen-suppressed, high-temperature environment. This study focused on the structural reconstructing during pyrolysis and its impact on the ammonia decomposition capabilities of the resulting metal oxide and Ru nanoparticle interactions. For Hf-MOF and Zr-MOF, the pyrolysis facilitated carbothermal reduction, transforming the organic ligands into conductive porous carbon and removing oxygen from the oxide clusters. This process resulted in the formation of highly crystalline oxide particles approximately 20 nm in size, with observable oxygen vacancies. Conversely, the pyrolysis of Ce-MOF exhibited a distinct behavior, significantly influenced by the strong adsorption of CO_2 molecules at the Ce^{3+} nodes. This interaction delayed structural collapse under high-temperature treatment, leading to the formation of smaller, approximately 5 nm CeO_2 particles without oxygen vacancies, as the adsorbed CO_2 was released as CO gas. The Ru nanoparticles, uniformly 2.35 nm as confirmed by STEM, were ideal for ammonia decomposition. However, the interaction with highly reducible CeO_2 particles led to the lowest observed turnover frequency (TOF) of 0.01 s^{-1} for the Ru-CeO_2/C catalyst. Post-reaction analysis showed that Ru-ZrO_{2-x}/C catalysts underwent a significant change, with the Ru-Ru coordination number increasing from 4.7 to 6.1, likely due to sintering caused by the hydrogen gas produced during the ammonia decomposition. In contrast, the Ru-CeO_2/C catalyst showed little change in Ru-Ru coordination numbers, but a notable increase in Ru-O bonding was detected, suggesting closer interactions between Ru particles and CeO_2, potentially facilitated by the expanded interface area between them. This study not only highlights the complex interplay between catalyst structure and reactivity but also underscores the significance of metal-oxide interactions in influencing catalyst performance. Understanding these interactions provides valuable insights into the design of stable, oxide-based catalysts for broader energy applications beyond ammonia decomposition.

Methods

Sample preparation. The synthesis procedure for ruthenium nanoparticles supported on transition metal oxides was conducted as follows: Stoichiometric amounts of $HfCl_4$ and $CeCl_3$, equal to 0.343 mmol of $ZrCl_4$ (0.40 g), along with the linker precursor benzene-1,4-dicarboxylic acid (0.285 g, 0.343 mmol), were dissolved in 100 mL of N,N-dimethylformamide (DMF) inside a 500 mL Teflon-capped glass jar. The solution was homogenized using ultrasound for approximately 1 minute. Subsequently, 3.5 mL of acetic acid (AcOH), serving as a modulator, was added to the solution and further dispersed by ultrasound for about 1 minute. The sealed jars were then placed in an oven and maintained at 120°C under static conditions for 24 hours. Upon completion, white precipitates were observed, which were isolated by centrifugation once the mixture had cooled to room temperature. The collected solids were washed with DMF to remove any unreacted precursors, followed by a solvent exchange with acetone conducted six times over three days. After thorough drying, ruthenium ions were impregnated into the pores of each MOF by simple soaking in an aqueous solution of Ru^{3+} ions. The impregnated MOF powders were subsequently dried again and placed in an alumina boat, which was then positioned in a tube furnace. Ultra-high purity argon (UHP Ar) was flowed through the furnace to exclude the air, and the materials were annealed at 950°C for 1 hour at a ramp rate of 6.2°C per minute.

Physical characterizations. Powder X-ray diffraction (XRD) patterns were obtained with a D8-Advances (Bruker AXS) diffractometer, equipped with a rotating anode and a Cu Kα radiation source ($\lambda = 0.15418$ nm). Field emission scanning electron microscopy (FE-SEM) was measured by JEOL 5400 (Japan). High-resolution transmission electron microscope (HR-TEM) was measured by JEOL ARM 200CF TEM (Japan), which was operated at 200 keV. This microscope was equipped with a probe corrector, a Gatan OneView camera, and two silicon drift detectors (SDDs) for Energy Dispersive X-Ray Spectroscopy (EDS). The area of a single SDD is 100 mm2 and the total solid angle for collection is approximately 1.7 sr. X-ray photoelectron spectroscopic (XPS) were measured at Keck-II/NUANCE facility at Northwestern University using a Thermo Scientific ESCALAB 250 Xi (Al Kα radiation, 1486.6 eV). An equipped electron flood gun was utilized prior to any scans to minimize charging effect. The peak energies of C-C component were calibrated by the C 1s peak at 284.8 eV. N_2 sorption isotherms were recorded at 77 K with a Belsorp mini II analyser (MicrotracBEL, Japan). Before measuring, the samples were degassed in vacuum at 80 °C for at least 48 h. The average total run time was 10 h. The Brunauer−Emmett−Teller (BET) methods were used to quantify specific surface areas (SSAs) which were calculated from adsorption isotherms collected over the relative pressure (P/P_0) range of 0 to 1. Scanning transmission electron microscope (STEM) was also carried out using Talos 80–300 microscope at 300 kV with a spherical aberration (Cs)-correction. Thermogravimetric analysis (TGA) experiments were performed on a Mettler Toledo TGA/DSC 1 Star^e System (Schwerzenbach, Switzerland) interfaced with a PC using Stare software (version 9.10). Samples were placed in alumina pans and heated at a rate of 1 °C min^{-1} from 25 to 800 °C under a UHP nitrogen. Ru content of samples was investigated through inductively coupled plasma spectrometry optical emission spectroscopy (ICP-OES, iCAP7600, Thermo, USA). EXAFS spectra on all samples were collected at the 5-BM-D bending magnet beamline of DND-CAT, at the Advanced Photon Source, Argonne National Laboratory. A Si(111) double-crystal monochromator was used for energy selection. The incident X-ray beam intensity was detuned to 50% of its maximum in order to minimize the presence of harmonics. Data were acquired in transmission/fluorescence mode using ionization chamber detectors (FMB-Oxford)/the PIPS detector (Canberra). A metal foil spectrum was acquired with each sample measurement for energy calibration. Samples were evenly dispersed onto Scotch tape, which was then folded to optimize sample thickness. Data analysis was performed using the Athena/Artemis/Hephaestus software package,[41] which makes use of IFEFFIT.[42]

Catalyst Performance. Measurements were recorded using a packed-bed flow reactor. The gases used for ammonia decomposition were UHP H_2 and 10% NH_3 balanced with He. The catalyst (~ 30 mg supported Ru NPs diluted with 800 mg SiO_2) was packed on quartz wool in a quartz reactor. The reaction temperature was controlled with a K-type thermocouple at the top of the catalyst bed. For temperature screening test, the temperature was ramped at 1 °C/min to 700 °C under 10 mL/min 10% NH_3 gas flow at 1 bar. For TOF tests, NH_3 flow rates were adjusted to limit the ammonia conversion to below 10% and all reactions were performed at 400 °C. The conversions were calculated based on N_2 formation and NH_3 consumption values, which were identified using an Agilent 7890A gas GC with FID detector having an Agilent J&W GC column. For the stability test, different amount of catalysts were used to control the conversion within a similar region under the same gas flow rate (10 sccm).

Supporting Information

Supporting Information is available from the Wiley Online Library or from the author.

Acknowledgements

Northwestern University, Institute for Catalysis in Energy Processes (ICEP), funded by DOE, Office of Science, Office of Basic Energy Sciences (DE-FG02-03ER15457). This work was supported by "Human Resources Program in Energy Technology" of the Korea Institute of Energy Technology Evaluation and Planning (KETEP), granted financial resource from the Ministry of Trade, Industry & Energy, Republic of Korea. (No. 20224000000410) The authors made use of the Northwestern University NUANCE Center and IMSERC Center, which are partially supported by the Soft and Hybrid Nanotechnology Experimental (SHyNE) Resource (NSF ECCS-2025633), the Materials Research Science and Engineering Center (NSF DMR-1720139), the state of Illinois, and Northwestern University. This research was supported by Basic Science Research Program through the National Research Foundation of Korea (NRF) funded by the Ministry of Education (grant RS-2024-00409390)

Conflict of Interest

The authors declare no conflict of interest.

Data Availability Statement

The data that support the findings of this study are available from the corresponding author upon reasonable request.

Received: ((will be filled in by the editorial staff))
Revised: ((will be filled in by the editorial staff))
Published online: ((will be filled in by the editorial staff))

References

[1] G. Pacchioni, H. J. Freund, *Chem. Soc. Rev.* **2018**, *47*, 8474.
[2] H.-Y. T. Chen, S. Tosoni, G. Pacchioni, *J. Phys. Chem. C* **2014**, *119*, 10856.
[3] C. T. Campbell, *Nat. Chem.* **2012**, *4*, 597.
[4] L. Lin, W. Zhou, R. Gao, S. Yao, X. Zhang, W. Xu, S. Zheng, Z. Jiang, Q. Yu, Y.-W. Li, *Nature* **2017**, *544*, 80.
[5] L. Zhang, K. Doyle-Davis, X. Sun, *Energy Environ. Sci.* **2019**, *12*, 492.

[6] M. Kim, S. H. Kim, J. Park, S. Lee, I. Jang, S. Kim, C. Y. Lee, O. J. Kwon, H. C. Ham, J. T. Hupp, N. Jung, S. J. Yoo, D. Whang, *Adv. Funct. Mater.* **2023**, *33*, 2300673.

[7] A. Bavykina, N. Kolobov, I. S. Khan, J. A. Bau, A. Ramirez, J. Gascon, *Chem. Rev.* **2020**, *120*, 8468.

[8] J. Guo, P. Chen, *Chem* **2017**, *3*, 709.

[9] F. Schüth, R. Palkovits, R. Schlögl, D. S. Su, *Energy Environ. Sci.* **2012**, *5*, 6278.

[10] J. C. Ganley, F. S. Thomas, E. G. Seebauer, R. I. Masel, *Catal. Lett.* **2004**, *96*, 117.

[11] A. M. Karim, V. Prasad, G. Mpourmpakis, W. W. Lonergan, A. I. Frenkel, J. G. Chen, D. G. Vlachos, *J. Am. Chem. Soc.* **2009**, *131*, 12230.

[12] W. Zheng, J. Zhang, H. Xu, W. Li, *Catal. Lett.* **2007**, *119*, 311.

[13] S.-F. Yin, Q.-H. Zhang, B.-Q. Xu, W.-X. Zhu, C.-F. Ng, C.-T. Au, *J. Catal.* **2004**, *224*, 384.

[14] S. J. Wang, S. F. Yin, L. Li, B. Q. Xu, C. F. Ng, C. T. Au, *Appl. Catal. B-Environ.* **2004**, *52*, 287.

[15] S. Zhou, S. Lin, H. Guo, *J. Phys. Chem. C* **2018**, *122*, 9091.

[16] H. Wu, Y. S. Chua, V. Krungleviciute, M. Tyagi, P. Chen, T. Yildirim, W. Zhou, *J. Am. Chem. Soc.* **2013**, *135*, 10525.

[17] X. Liao, X. Wang, F. Wang, Y. Yao, S. Lu, *J. Inorg. Organomet. Polym. Mater.* **2021**, *31*, 756.

[18] Z. Guo, Q.-C. Luo, L. Qin, Z. Tian, Y.-Z. Zheng, Y. Ma, Y. Qu, *Inorg. Chem.* **2022**, *61*, 9557.

[19] F. C. Calaza, T.-L. Chen, D. R. Mullins, Y. Xu, S. H. Overbury, *Catal. Today* **2015**, *253*, 65.

[20] W. O. Gordon, Y. Xu, D. R. Mullins, S. H. Overbury, *Phys. Chem. Chem. Phys.* **2009**, *11*, 11171.

[21] M. Stawowy, M. Róziewicz, E. Szczepańska, J. Silvestre-Albero, M. Zawadzki, M. Musioł, R. Łuzny, J. Kaczmarczyk, J. Trawczyński, A. Łamacz, *Catalysts* **2019**, *9*, 309.

[22] J. N. Tiwari, A. M. Harzandi, M. Ha, S. Sultan, C. W. Myung, H. J. Park, D. Y. Kim, P. Thangavel, A. N. Singh, P. Sharma, S. S. Chandrasekaran, F. Salehnia, J. W. Jang, H. S. Shin, Z. Lee, K. S. Kim, *Adv. Energy Mater.* **2019**, 1900931.

[23] R. Tu, Z. Liu, C. Wang, P. Lu, B. Guo, Q. Xu, B.-W. Li, S. Zhang, *RSC Adv.* **2022**, *12*, 15555.

[24] W. Zheng, J. Zhang, B. Zhu, R. Blume, Y. Zhang, K. Schlichte, R. Schlögl, F. Schüth, D. S. Su, *ChemSusChem* **2010**, *3*, 226.

[25] A. Chatterjee, S. Pradhan, A. Datta, M. De, D. Chakravorty, *J. Mater. Res.* **1994**, *9*, 263.

[26] W. Cao, W. Luo, H. Ge, Y. Su, A. Wang, T. Zhang, *Green Chem.* **2017**, *19*, 2201.

[27] K. Deori, D. Gupta, B. Saha, S. K. Awasthi, S. Deka, *J. Mater. Chem. A* **2013**, *1*, 7091.

[28] L. M. Berger, W. Gruner, E. Langholf, S. Stolle, *Int. J. Refract. Met. Hard Mat.* **1999**, *17*, 235.

[29] P. Lackner, Z. Zou, S. Mayr, U. Diebold, M. Schmid, *Phys. Chem. Chem. Phys.* **2019**, *21*, 17613.

[30] Y. Zhang, J. Xu, D.-Y. Zhou, H.-H. Wang, W.-Q. Lu, C.-K. Choi, *Chin. Phys. B* **2018**, *27*, 048103.

[31] Z. Wang, R. Lin, Y. Huo, H. Li, L. Wang, *Adv. Funct. Mater.* **2022**, *32*, 2109503.

[32] Z. Wang, Z. Huang, J. T. Brosnahan, S. Zhang, Y. Guo, Y. Guo, L. Wang, Y. Wang, W. Zhan, *Environ. Sci. Technol.* **2019**, *53*, 5349.

[33] Y. Guo, S. Mei, K. Yuan, D.-J. Wang, H.-C. Liu, C.-H. Yan, Y.-W. Zhang, *ACS Catal.* **2018**, *8*, 6203.

[34] Z. Hu, Y. Wang, D. Zhao, *Chem. Soc. Rev.* **2021**, *50*, 4629.